A Wireless-Enabled Microdischarge-Based Radiation Detector Utilizing Stacked Electrode Arrays for Enhanced Detection Efficiency

Christine K. Eun and Yogesh B. Gianchandani, *Fellow, IEEE*

***Abstract*—This paper describes a wireless gas-based beta/gamma radiation detector that uses an arrayed electrode structure to demonstrate a scalable path for increasing detection efficiency. The device uses an assembly of stainless-steel electrodes and a glass spacer structure within a TO-5 package. The components are manufactured by commercial micromachining methods, e.g., the electrodes are photochemically etched whereas the spacer structure is ultrasonically machined. Two different fill gases are evaluated near 760 torr—i.e., Ar and P-10. The detector diameter and height are 9 and 9.6 mm, respectively, and its weight is 1.01 g. With a 99-μCi Cs-137 source (which is a beta and gamma emitter), the detector provides $>$ 78 cpm to a hardwired interface at a source-detector distance of 30.5 cm. Receiver operating characteristics evaluated for integration times ranging from 30 to 180 s have shown to improve with longer integration time. The estimated intrinsic detection efficiency (i.e., with the background rate subtracted) is $\approx$4%, as measured with the biasing arrangement described in this paper. Portable powering modules developed for these detectors are also presented. During operation, gas microdischarges between the electrodes, which are initiated by incident radiation, transmit wideband wireless signals. Wireless signaling has been demonstrated to exhibit fast transient durations on the order of tens of nanoseconds. Wireless-enabled radiation sensors are envisioned for use in rapidly deployable mobile network configurations. [2010-0362]**

***Index Terms*—Ar, beta particles, gamma radiation, microdischarges, P-10, wireless transmissions.**

I. Introduction

MINIATURIZED detectors can serve applications ranging from monitoring leakage and stray radiation in power plants and medical facilities to providing first-alert information for homeland security. The wireless signaling capability can facilitate sensor networks [1], [2]. In addition, leveraging scalable manufacturing processes and well-established packaging platforms can enable cost-effective, rapid-prototyping, and large-scale manufacturing.

Gas-based detectors (e.g., Geiger counters) are often favored for environmental surveillance efforts (e.g., in looking for radiation leaks and inadvertent contamination) [3]. These are relatively simple and robust and can operate over a large temperature range and measure a wide range of radiation species and energies. The basic structure of a detector includes two biased electrodes (an anode and a cathode) enclosed within a gas-filled chamber. Beta particles directly interact with the gas, causing avalanche discharges, with current pulses that register as "counts." Under appropriate conditions, electrical discharges such as these can emit broadband radio-frequency radiation in the manner of Marconi transmitters [4]. It has been shown that even microdischarges can be used for wireless signaling [5].

Oftentimes, when a radioisotope undergoes decay, a combination of radiation types is emitted. For example, when ^{137}Cs decays, it emits beta particles (with an endpoint energy of 514 keV) 94.4% of the time and gamma rays (with an energy of 662 keV) 85.1% of the time [6]. This type of radiation source may be detected by either a beta detector or a gamma detector. Of course, a detector that is responsive to both beta and gamma radiation is likely to measure a higher signal from such a source.

Gas-based detection of gamma radiation relies on converting the photons into photoelectrons and detecting the ejected photoelectrons [7]–[10]. Detection is often facilitated by using high-density metals for the electrodes and for the walls encapsulating the fill gas. The use of high-pressure fill gases that have large atomic numbers [11], [12] can also increase the interaction probability. Gamma radiation interacts with materials in primarily three collision processes, i.e., the photoelectric effect, Compton scattering, and pair production. The energy of the incoming photon determines the collision process. Collisions involving low-energy photons are dominated by the photoelectric effect, where the impinging photon transfers all of its energy to an ejected photoelectron. Collisions of higher energy photons (but $\mathrm{E} < 1.022$ MeV) cause Compton scattering, in which a photoelectron and a secondary photon are emitted. For incident photons with $\mathrm{E} > 1.022$ MeV, the collision process is dominated by pair production, where a high-energy electron and a positron are ejected. The positron is quickly annihilated by a free electron, resulting in the emission of two photons with identical energies of 0.51 MeV.

One inherent limitation of gas-based detectors is the low density of the gaseous detection medium, which results in low detection efficiencies (1%–3%), particularly for gamma and neutron radiation [3], [13]. Utilizing multiple stacks of a detector structure can potentially increase detection efficiencies for a device with a given form factor.

Manuscript received December 28, 2010; accepted February 7, 2011. Date of publication April 7, 2011; date of current version June 2, 2011. This work was supported in part by the Department of the Army, Micro Autonomous Systems and Technology Collaborative Technology Alliance, under Contract W911NF-08-2-0004. Subject Editor N. F. de Rooij.

The authors are with the Department of Electrical Engineering and Computer Science, University of Michigan, Ann Arbor, MI 48109 USA (e-mail: eunc@umich.edu).

Color versions of one or more of the figures in this paper are available online at http://ieeexplore.ieee.org.

Digital Object Identifier 10.1109/JMEMS.2011.2127461

Past work on stacking detector structures in order to achieve improved performance includes a variation on the gas electron multiplier (GEM) [14]. The GEMs use an insulating film (50–100-μm-thick polyimde) with a thin metal laminate (1–5 μm thick) on both sides. The structures are perforated, with openings 25–150 μm in diameter spaced apart by 50–200 μm [14], [15]. An applied voltage generates concentrated electric fields (50–70 kV/cm) at the edges of the perforations, which accelerates the ionized particles through the openings. Each perforation acts as an independent proportional counter. The triple GEM detector utilizes the parallel stacking of three GEM structures in order to increase the amplification of the carriers (or gain) at lower bias conditions (as compared with a single GEM). These GEM stacked structures require several bias voltages (for each layer of GEM, as well as for the drift and readout plate) for proper operation.

This paper evaluates a scalable path for increasing detection efficiency by utilizing a 3-D micromachined structure with a perimeter-supported stack of electrodes.[1] This approach maximizes the overall effective sensitive volume for a given detector by increasing the number of sensing gaps, increasing the amount of high-Z materials for gamma interaction, and utilizing the entire volume of a given package (for this effort, a TO-5 header). Only one electrical bias is utilized. This structure builds upon a previous effort in which a single anode–cathode pair was evaluated [17].

In this paper, Section II details the device concept. Section III describes the fabrication and assembly process, followed by Section IV, which details the experimental results. Section V discusses the results and impact of this work.

II. Device Concepts and Operation

The detector structure includes two sets of perforated stainless-steel #304 electrode arrays. The anode has four elements, and the cathode has three elements. The elements in each set are connected by v-shaped links. Each set is designed to be plastically deformed into a stack of parallel elements. These elements are inserted into an insulating glass structure with micromachined shelves, which maintain a 200-μm-wide anode–cathode gap spacing (Fig. 1). The glass structure and steel elements are installed onto a TO-5 header base using the package pins for stability and electrical access. The electrode assembly is contained within a glass cylinder of 1-mm wall thickness and capped by a glass lid of 50-μm thickness. An applied bias generates high-field regions near the perforations. The detector structure is surrounded by a fill-gas environment (e.g., either 100% Ar or an Ar-CH_4 mixture) near 760 torr. Beta radiation directly interacts with the fill gas, whereas gamma radiation mostly interacts with the steel electrodes to generate photoelectrons. Beta radiation or photoelectrons initiate current-driven avalanche pulses between the biased electrodes, which transmit wideband wireless signals.

Assuming that the gamma source forms a narrow beam of photons and this beam interacts with the electrode material

[1]Portions of this paper have been reported in conference abstract form in [16].

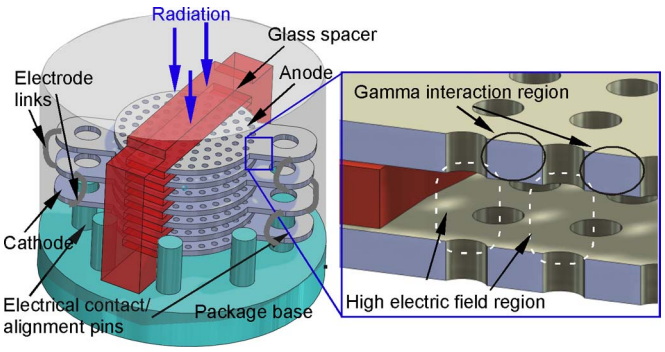

Fig. 1. *Device concept*. The detector comprises a stacked arrangement of multielectrode stainless-steel elements (i.e., anode and cathode) and a glass insulator, assembled within a commercial TO-5 package base. Each electrode is an array of three or four "linked" elements. Machined shelves within the spacer maintain a 200-μm-wide gap spacing between each electrode layer. Gamma radiation interacts with the metal layers, which releases photoelectrons into the biased gap. These charged particles trigger an avalanche within the biased gap, leading to wireless signaling.

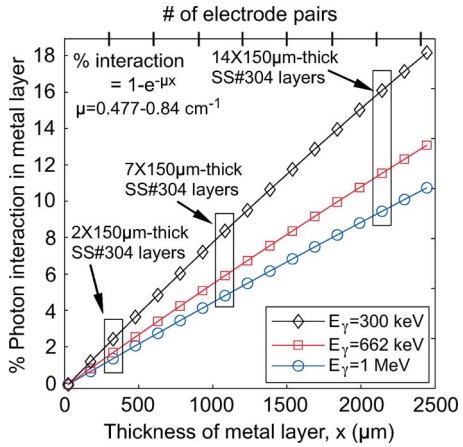

Fig. 2. Estimated percentage photon interaction as a function of metal thickness. As the number of metal layers increases, the higher becomes the potential detection efficiency. Three photon energies are evaluated: 300 keV, 662 keV, and 1 MeV. As energies increase, the likelihood of photon interaction with the metal (e.g., stainless steel #304) decreases. The linear attenuation coefficient μ ranged from 0.477 to 0.84 cm^{-1}. Photon interactions can occur in either the anode or cathode.

to generate one photoelectron per gamma radiation (i.e., the photoelectric effect), then the estimated percentage of detected photons is

$$\%\text{photon interaction} = 100 \times \left(1 - B(x, E_\gamma)e^{-\mu x}\right) \qquad (1)$$

where μ is the linear attenuation coefficient (in per centimeter) of the electrode material, x (in centimeters) is the thickness of the electrodes, and B is the buildup factor [3]. For steel, the collision processes are dominated by the photoelectric effect and Compton scattering [18]. In order to eject a photoelectron from the surface of a metal layer, the incident photon must have an energy greater than the work function of the metal surface. Typical work function energies range from 4 to 6 eV [19]. The buildup factor corrects for the fraction of scattered gamma rays that are retained in the photon beam [3]. The magnitude of the buildup factor depends on the absorber material, thickness, and photon energy [20]. For these calculations, B is assumed to be unity.

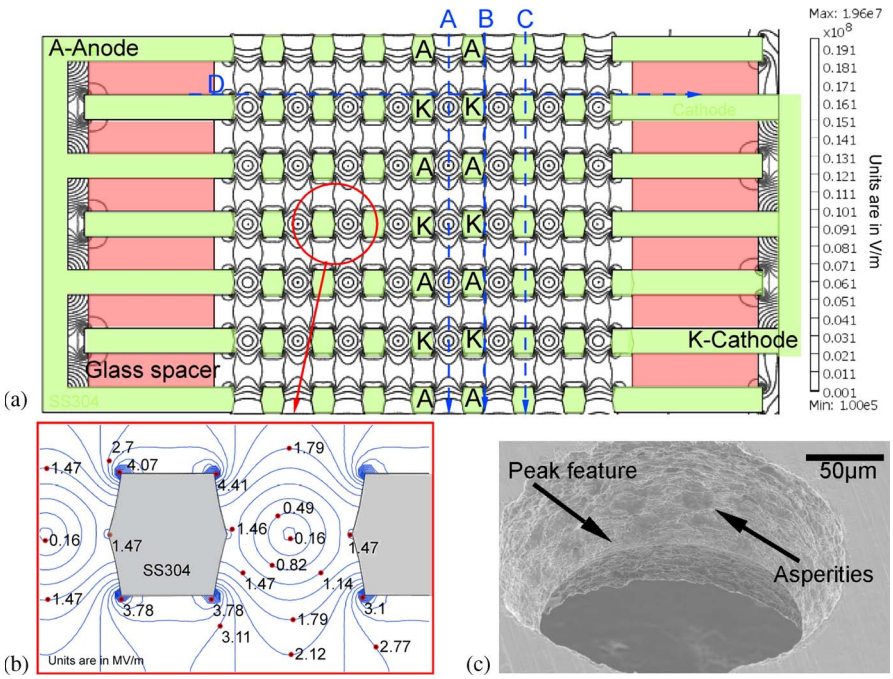

Fig. 3. (a) Cross-sectional view of 2-D finite-element modeling of the electrode field generated in the electrode array stack. $Vapplied = 600$ V. (b) Magnified view of the field profile near the peaked feature. Units are in megavolts per meter. (c) SEM photographs of the perforations show a top diameter of 225 μm and center diameter of 175 μm.

The estimated percentage of photons that interact with the structure is calculated as a function of metal thickness (Fig. 2). Three photon energies were evaluated for stainless steel #304, i.e., 300 keV, 662 keV (which corresponds to a ^{137}Cs source), and 1 MeV. For two metal layers, the estimated photon interaction using a ^{137}Cs source is 1.5%–2.0%. As the number of metal layers increases (e.g., seven metal layers), the higher becomes the potential detection efficiency (6%–7%). Lower photon energies result in higher interaction percentages for a given electrode material and thickness. For example, 300-keV photons have 1.5–1.8$\times$ greater interaction probabilities compared with 662 keV and 1 MeV. The gamma intensity attenuation through the 1-mm-thick glass sidewalls and 50-μm-thick glass lid were 1.5% and less than 0.1%, respectively. The beta energy attenuation through the sidewalls and lid were 380 keV and less than 9.52 keV, respectively.

A. Electric Field Modeling

Finite-element analysis using COMSOL 3.5a was used to model the electric field profile of the arrayed electrode configuration [Fig. 3(a)]. The simulations show that with a 200-μm gap spacing and a bias level of 600 V, a maximum electric field of approximately 4–5 MV/m is generated near the perforation corners. Fig. 3(b) shows a magnified view of the field profile near a perforation. The wet etching process that forms the perforations results in a slight sloped profile and a peaklike feature at the center of the perforation. There is a 50-μm difference in hole diameter from the top of the perforation to its center. Compared with straight sidewalls, these peak features result in increased field strengths (that is approximately 75% higher for a given bias voltage) within the perforation. A SEM photograph illustrates the peak feature [Fig. 3(c)].

One-dimensional field profiles following different paths through the detector were modeled for a range of applied biases (Fig. 4). Fig. 4(a) shows Line A following a vertical path through the center of the perforations. The impact of applied bias is most pronounced at the peak features. Fig. 4(b) shows Line B following a vertical path near the edge of the perforations (passing through the peak features) and shows a maximum field of 2.75 MV/m for a 600-V bias. Fig. 4(c) shows Line C following a vertical path through the center of the electrodes. The highest field concentrations occurred near the corner edges of the electrodes, which showed a maximum field between 4 and 5 MV/m [Fig. 4(d)].

III. Fabrication and Assembly

The detector elements are manufactured by commercial processes. In particular, the electrodes are formed by photochemical machining of steel foil (Kemac Technology, CA), whereas the glass spacers are formed by ultrasonic machining (Bullen Ultrasonics, OH). To fabricate the electrodes, dry photoresist is laminated on both sides of 150-μm-thick stainless steel (#304). Following double-sided lithography, the sample is through-etched by a hot etchant spray. In this particular design, 175-μm-diameter circular perforations are formed, with 300-μm center-to-center spacing. The glass spacer is formed by ultrasonically machining a 1.14-mm-thick borosilicate-glass substrate. During the machining process, a lithographic mask is used to pattern the glass substrate. The machined grooves in the spacer are 200 μm thick and separated by 200-μm gaps.

The assembly of the device is executed in-house. Each electrode array begins planar [Fig. 5(a)] and has been designed to plastically deform at the links, similar to an accordion pattern. This results in a parallel configuration of electrode elements

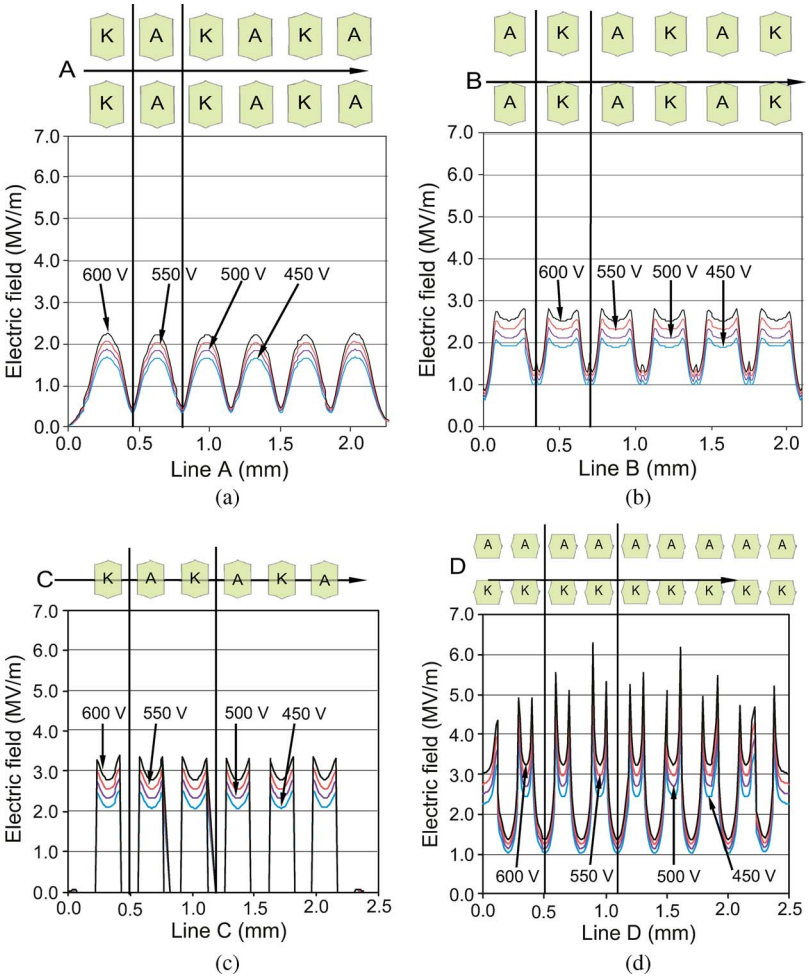

Fig. 4. Electric field profiles of different regions of the electrode array for applied biases ranging from 450 to 600 V. (a) Line A follows vertically along the center of the perforations. (b) Line B follows vertically along the edge of the electrode. (c) Line C follows vertically through the center of the electrodes. (d) Line D follows horizontally along the top edge of a cathode layer. The same vertical scale is used in all four plots to allow easy comparison. The highest field concentrations occur near the corner edges of the electrodes.

with each element separated by approximately 600 μm [Fig. 5(b)]. The links provide structural stability and help maintain the element–element separation. In addition, these provide a continuous electrical connection for the entire array, simplifying bias requirements during operation. The first modified electrode array (i.e., the anode) is carefully inserted into the glass spacer [Fig. 5(c)], followed by the cathode array. Each electrode element is aligned with a spacer shelf. The pair of electrode arrays is interdigitated with alternating anode and cathode elements. To facilitate assembly, the spacer shelves are 50 μm taller than the thickness of the electrodes. In addition, each steel element is designed with openings to align with the package pins. These pins provide electrical contact to the electrodes. The glass spacer fits between adjacent pins [Fig. 5(d)]. The package is a commercial eight-pin TO-5 metal header with a 9-mm diameter and 9.6-mm height. The pins serve as electrical feedthroughs through the package base.

IV. Experimental Results

The testing configuration is shown in Fig. 6. A printed circuit board (PCB) module was designed to power the device and interface with the measurement equipment. The required components for the powering module included a battery source, an adjustable voltage regulator, a high-voltage converter, the detector bias circuitry, and a readout element (Fig. 7). The voltage regulator provided a dc input (that was adjustable from 0 to 5 V) for the high-voltage converter, which linearly amplified the dc voltage from 0 to 2000 V. The output of the converter was applied to the detector bias circuitry, which consisted of a 5-pF capacitor and various ballast resistors to manage the discharge current. An optical readout offered instantaneous and reliable optical signaling without additional wiring or measurement equipment. Positioning the LED in the current path of the detector assured that each triggered event generated an optical signal.

For this paper, the detectors were not hermetically packaged, but as noted in Section II, the electrode assembly was contained within a glass enclosure with 1-mm-thick sidewalls and a 50-μm-thick lid (Fig. 6). The enclosure featured an inlet and an outlet port for gas flow, which enabled the testing of various fill gases, e.g., Ar and P-10. In a typical test procedure, the enclosure was positioned above the TO-5 package base, encapsulating the detector structure. It was sealed onto the detector

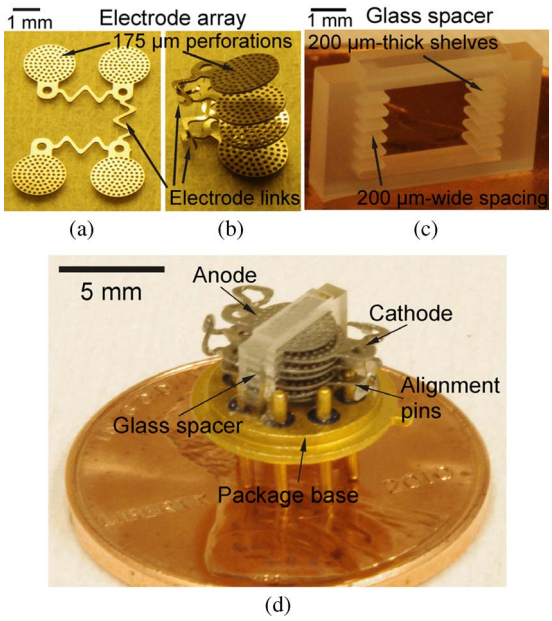

Fig. 5. *Device assembly*. (a) Beginning with a planar arrangement of linked elements, (b) each element is folded at the link to create an accordion pattern. (c) Micromachined glass spacer has seven pairs of slotted shelves to house the electrode arrays. (d) Folded anode and cathode are placed within the glass spacer, separated by machined shelves and into the package base using the alignment pins.

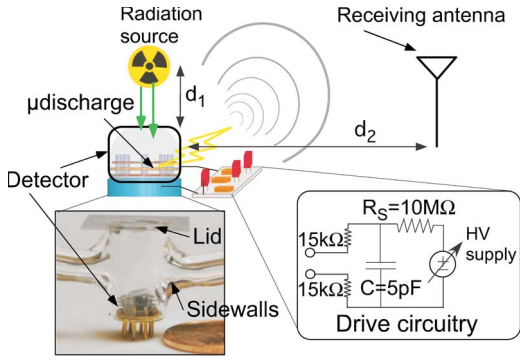

Fig. 6. Test setup with the device and bias circuitry (positioned at distance d_1 from the radiation source). *Wireline* measurements of the current pulses were taken at the cathode with a high-frequency inductive current probe attached to an oscilloscope. *Wireless* measurements were taken with a receiving antenna attached to an oscilloscope at distance d_2 from the detector.

TO-5 base with epoxy; the inlet port was attached to the gas regulator, while the outlet port was attached to the pressure sensor and roughing pump. Valves were used to regulate the gas flow and pressure inside the glass enclosure and detector structure. A constant volumetric mass flow rate of 60 standard cubic centimeters per minute (sccm) of the fill gas was used. It was operated under these minimal flow conditions in order to purge possible contaminants that may have leaked through the epoxy seal and ensured purity of the fill gas. The detector structures were characterized with a small 99-μCi radiation source of ^{137}Cs. (This corresponds to gamma and beta emission rates of approximately 1.86×10^8 and 2.07×10^8 particles per minute, respectively.) The radiation source was positioned above the glass lid, minimizing the attenuation. Wireline measurements

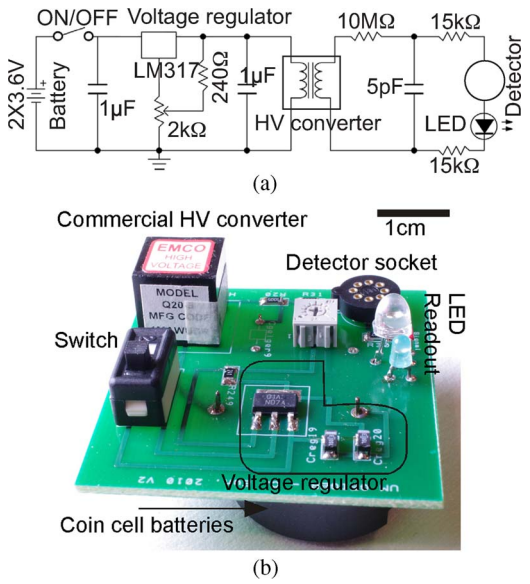

Fig. 7. (a) Circuit schematic and (b) populated PCB of an HV powering module for the detector. It included coin cell batteries, a voltage regulator circuit, the commercial high-voltage converter, the detector bias circuit, and an optical readout. The total PCB weighs 26.5 g.

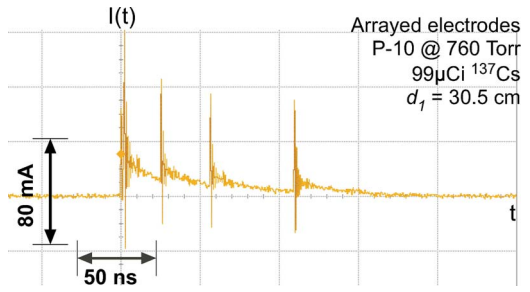

Fig. 8. Oscilloscope trace of the current pulses with 100–150-ns duration.

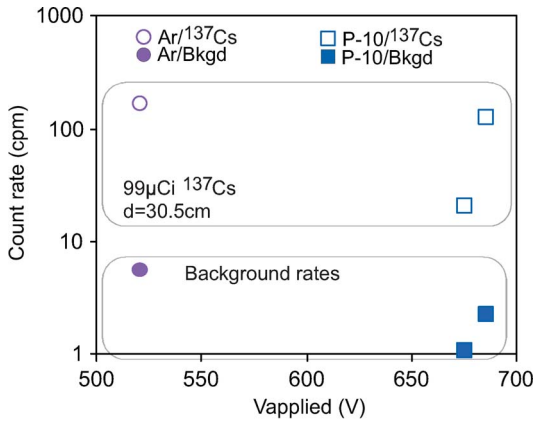

Fig. 9. Count rates as a function of applied bias and fill gases. Two fill gases were examined, including the P-10 fill gas (i.e., 90% Ar and 10% CH_4) and Ar with a 60-sccm flow rate near 760 torr. Background rates increased at a slower rate.

of the count rate were provided by a high-frequency inductive current probe attached to an oscilloscope (Agilent DSO8064A, 600 MHz). The wireless transmissions were measured by the same oscilloscope connected to an 800-MHz whip antenna.

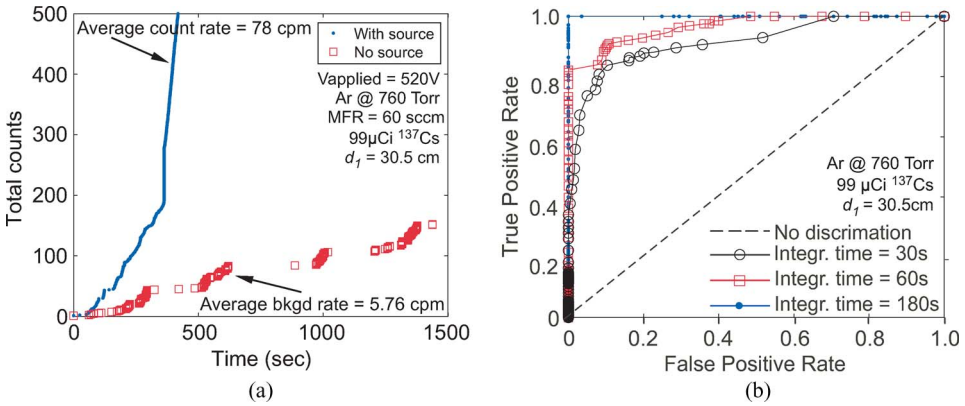

Fig. 10. (a) Distribution of counts in time with and without a source present. The average count rate and background rate were approximately 78 and 5.76 cpm, respectively. (b) ROC curves for various integration times ranging from 30 to 180 s.

A. Wireline Measurements

Typical current discharge pulses are of 100–150-ns duration and are comprised of multiple smaller peaks with 25–50-ns duration and 100-mA amplitude (Fig. 8). The applied biases for the detector ranged from 500 to 575 V for a pure Ar fill gas and 675 to 775 V for a P-10 fill gas (90% Ar and 10% CH_4) operating near 760 torr. Fig. 9 shows the impact of applied bias on counting rates. At a 520-V bias with Ar fill gas, typical count rates were near 170 counts per minute (cpm) at a 99-μCi ^{137}Cs-to-detector distance of 30.5 cm. At a 685-V bias and a P-10 fill gas, typical count rates were near 127 cpm. Measured background rates (i.e., in the absence of a radiation source) ranged from 1.1 to 5.8 cpm. The rates while operating with P-10 increased 6× for a 10-V increase in applied bias. In comparison, the background counts were not as sensitive to bias and only doubled.

ROC Curves: The receiver operating characteristic (ROC) curve depicts the compromise between successful detection events and false-alarm rates [3], [21], [22]. The impact upon the ROC curves of sensor integration time over which detection counts are collected was evaluated. The true positive rate (TPR) is the fraction of true detection events (i.e., when a source is present) above a predetermined threshold of counts. The false positive rate (FPR) is the fraction of detection events above the same threshold without a source present, i.e., background events. Integration time is the measurement time window during which the device is collecting detection events or "counts."

Each point on the ROC curve corresponds to an (FPR, TPR) value for a particular threshold. For example, at TPR $= 0.5$, 50% of the detected events will be true detection events and the corresponding FPR value on the curve is the fraction of false-alarm events. For superior performance, the TPR must approach 1 at a low value of FPR.

ROCs were calculated (using MATLAB 7.11) for these detector structures. Detection events were recorded as a function of time for a bias voltage of 520 V [Fig. 10(a)]. The source–detector distance was fixed at 30.5 cm. The time stamps for each triggered event were stored using the segmented acquisition mode on the oscilloscope. The slopes of the curves provided estimates of the counting rates. The steplike behavior was due to counts appearing in clusters or bursts. The typical count rate in the presence of the source was approximately 13.5× the background rates.

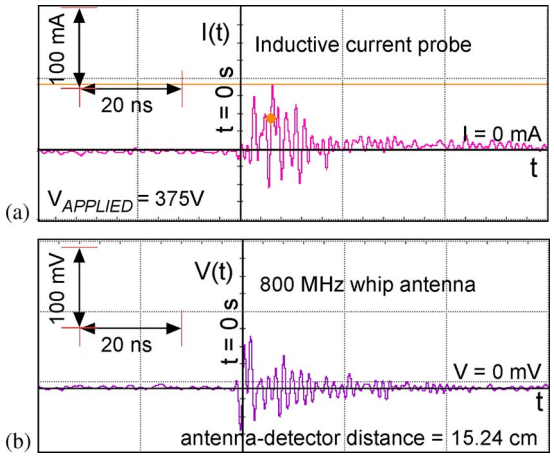

Fig. 11. (a) Current pulse measurement (of a "count") showed approximately 100-mA peaks and 20–50-ns duration. (b) Transmitted wireless signal was received using an 800-MHz whip antenna attached to an oscilloscope. The antenna–detector distance was 15.24 cm. The time domain behavior of the RF transmission followed closely with the current pulse measurement. From ^{137}Cs, 99 μCi was used.

The intrinsic detector efficiency $\varepsilon_{\rm int}$ is defined as the percentage of radiation incident on the detector that results in recorded pulses [3]. Assuming a point isotropic source of activity A (in curies), a source–detector distance d_1 (in meters), and a detector surface area (i.e., facing the direction of the source) S_D (in square meters), then $\varepsilon_{\rm int}$ can be rewritten as

$$\varepsilon_{\rm int} = \frac{\text{Measured count rate (cpm)}}{A \cdot 60 \cdot 3.7 \times 10^{10} \cdot \frac{S_D}{4\pi \cdot d_1^2}}. \tag{2}$$

The gamma and beta fluence rates were approximately 1904 and 2112 particles per minute per square meter, respectively. The majority of the counts are attributed to gamma radiation because the top metal layers attenuate a significant portion of the beta radiation without leading to measured counts. (The perforations, which are the regions where the beta radiation can ionize the fill gas, cover only 15% of the electrode area.) Assuming predominantly gamma detection, the corresponding intrinsic detection efficiency is ≈4%.

TABLE I
COMPARISON OF THE ARRAYED DETECTOR STRUCTURE WITH A COMMERCIAL GM TUBE

	COTS GM tube (LND 726)	Multi-stacked Array Detector
Gas filling	Ne + Halogen	Ar
Cathode material	446 Stainless Steel	304 Stainless Steel
Maximum length (mm)	49.8	9.6
[1]Effective length (mm)	10.2	0.90
Max. diameter (mm)	8.7	9
[1]Effective diameter (mm)	6.4	1.94
Volume (mm^3)	328	10.62
Operating voltage range (volts)	660 - 800	480 - 520
Gamma sensitivity (cpm/mR/hr)	210	227.4[2]
[3]Normalized gamma sensitivity (cpm/mR/hr/mm^3)	0.6 -calibrated with ^{60}Co or unknown strength.	21.6 -calibrated with 99 μCi ^{137}Cs at d = 30.5 cm
Background rates	10 cpm (shielded, with 50mm Pb + 3mm Al)	5-6 cpm (unshielded)
Maximum measured detection efficiency for 99μCi at d=30.5 cm (%)	N/A	≈4%
Weight (grams)	10	1.01

[1] *Effective length/diameter refers* to active/sensitive region of detector
[2] Measured at an exposure rate of 0.343 mR/hr.
[3] Normalized to detector sensitive volume - volume between anode/cathode.

Fig. 10(b) shows the ROC curves from the data shown in Fig. 10(a). As integration times increased, the receiver characteristics improved. An integration time of 180 s resulted in an ROC curve approaching the ideal ROC curve (FPR $= 0$, TPR $= 1$). For an integration time of 60 s, the threshold values for TPR $= 0.5$ and FPR $= 0.5$ were 78 and 6 counts, respectively. This indicated that the number of measured counts with a source present were typically $13\times$ the background counts. The most favorable operating points appeared to be at FPR values ranging from 0.1 to 0.2. As integration times increased from 30 to 180 s, the likelihood of a true detection event increased from 80% to near 100% for a corresponding FPR near zero.

B. Wireless Measurements

The current pulse measurement showed 20–50-ns duration [Fig. 11(a)], which was similar in behavior to the transmitted wireless spectra [Fig. 11(b)] received using a commercial 800-MHz whip antenna. The antenna was 30.5 cm in length and positioned at an antenna–detector distance of 15.24 cm, perpendicular to the ground. The receiving antenna was able to receive transmitted pulses at a rate similar to the wireline count rates. The received signal attenuated with increasing antenna–detector distance.

V. DISCUSSION AND CONCLUSION

The use of multiple vertically stacked electrode layers has been previously reported, e.g., the triple GEM structure [14], [15]. This structure was operated at a lower bias field and intended to proportionately amplify charge carriers. The carriers were accelerated from one GEM layer to the next, which required multiple voltage biases. In contrast, the structure described here is operated at a higher bias, in the Geiger–Muller regime. The interdigitated arrayed electrodes, which require only a single bias level, serve to increase the gamma detection efficiency. The stacked electrodes also increase the photon–photoelectron conversion efficiency, which increases the overall gamma sensitivity.

Operating voltages were higher with P-10 fill gases than with pure Ar. This is consistent with expectations: the polyatomic quench gas, methane, absorbs UV photons generated during the avalanche process, which, otherwise, would go on to create additional ionizations. Therefore, a larger electric field is required to generate enough avalanching for comparable discharge operation [23], [24]. The addition of the methane in the Ar fill gas can increase operational stability (i.e., accommodate a wider range of operating voltages) and decrease spurious discharges. In particular, the presence of a quench gas can alleviate the sensitivity of bias conditions that is caused by electric field concentrations. However, methane can also introduce a few complications. For example, it is flammable and also eventually becomes consumed in the fill gas [3]. Typical detectors filled with P-10 operate with lifetimes on the order of 10^6-10^8 total counts. For particularly high-count rate applications, this can truly be a limiting factor. In addition, a byproduct of the discharge process is a polymer film, which can be deposited on the electrodes, creating a barrier to future discharges. The use of halogen quench gases can alleviate these issues of lifetime and byproducts, but can be corrosive to certain metals. Platinum coatings are sometimes used to protect the electrode structures.

In this effort, elements for stacked detectors were manufactured by commercial micromachining technologies, particularly photochemical etching of the electrodes and ultrasonic machining of the spacer structure. The elements were then assembled within commercial packages to form seven stacked electrode arrays for gamma and beta detection. The detector diameter and height were 9 and 9.6 mm, respectively, and the weight was 1.01 g. The device performance was characterized using two fill gases (i.e., Ar and P-10) near 760 torr, with a 99-μCi ^{137}Cs source (which is a beta and gamma emitter). It demonstrated outputs > 78 cpm with a source–detector distance of 30.5 cm.

The performance of the multistacked arrayed detector compared with a commercial Geiger–Muller detector is summarized in Table I. The arrayed detector displayed a gamma sensitivity that was slightly better than the commercial unit and, when normalized to detector sensitive volume, performed 30× higher. The detector sensitive volume is the total volume encapsulated between the anode and cathode. (The arrayed detector volume was only 3% the volume of the commercial device.) The background rates from the microdetectors were lower than the commercial unit, which was expected since the Geiger–Muller detector has a much larger sensing volume. Comparing the arrayed detector with the single anode–cathode configuration described in a previous effort [17], the arrayed detector had a volume 6× greater than the single-stacked one and the arrayed detector contained 2.3× more electrode layers. The arrayed detector demonstrated gamma sensitivities that were proportionately higher (6×) compared with those of the single-stacked configuration.

Wireless signaling during detector operation exhibited fast transient durations on the order of tens of nanoseconds. Peak detection was used to discriminate the received wireless signal from the background noise floor. The background RF noise had amplitudes in the range of 10–20 mV (compared with the 50–100-mV peaks). Large static discharges in the vicinity of the receiver antenna may contribute to false positives.

ROCs evaluated for integration times ranging from 30 to 180 s showed improvement with longer integration time. The estimated intrinsic detection efficiency (i.e., with the background rate subtracted) was ≈4%. Portable powering modules developed for these detectors were also presented. Wireless-enabled radiation sensors are envisioned for use in rapidly deployable mobile network configurations.

REFERENCES

[1] R. J. Nemzek, J. S. Dreicer, D. C. Torney, and T. T. Warnock, "Distributed sensor networks for detection of mobile radioactive sources," *IEEE Trans. Nucl. Sci.*, vol. 51, no. 4, pp. 1693–1700, Aug. 2004.

[2] R. Kyker, N. Berry, D. Stark, N. Nachtigal, and C. Kershaw, "Hybrid Emergency Radiation Detection (HERD), a wireless sensor network application for consequence management of a radiological release," *Proc. SPIE*, vol. 5440, pp. 293–304, 2004.

[3] G. F. Knoll, *Radiation Detection and Measurement*. Hoboken, NJ: Wiley, 2000.

[4] J. E. Brittain, "Electrical engineering Hall of Fame: Guglielmo Marconi," *Proc. IEEE*, vol. 92, no. 9, pp. 1501–1504, Aug. 2004.

[5] C. K. Eun, R. Gharpurey, and Y. B. Gianchandani, "Wireless signaling of beta detection using microdischarges," *J. Microelectromech. Syst.*, vol. 19, no. 4, pp. 785–793, Aug. 2010.

[6] R. B. Firestone and L.P. Ekstrom, "LBNL Isotopes Project," *LUNDS Universitet*, Ver. 2.1, Feb. 1999. [Online]. Available: http://ie.lbl.gov/toi/index.asp

[7] B. S. Sheinfux and A. Seidman, "High efficiency gamma-ray metal converters," *Nucl. Instrum. Methods*, vol. 129, no. 1, pp. 177–186, Nov. 1975.

[8] U. Shimoni, B. Sheinfux, A. Seidman, J. Grinberg, and Z. Avrahami, "Investigations on metal converters for gamma-ray detection and mapping," *Nucl. Instrum. Methods*, vol. 117, no. 2, pp. 599–603, May 1974.

[9] M. Nakamura, "The energy spectra and the quantum efficiencies of electrons emitted from the metallic elements irradiated by ^{60}Co gamma-rays," *J. Appl. Phys.*, vol. 54, no. 6, pp. 3141–3149, Jun. 1983.

[10] J. O. Hirschfelder, J. L. Magee, and M. H. Hull, "The penetration of gamma-radiation through thick layers," *Phys. Rev.*, vol. 73, no. 8, pp. 852–862, Apr. 1948.

[11] C. E. Lehner, Z. He, and G. F. Knoll, "Intelligent gamma-ray spectroscopy using 3-D position-sensitive detectors," *IEEE Trans. Nucl. Sci.*, vol. 50, no. 4, pp. 1090–1097, Aug. 2003.

[12] S. D. Kiff, Z. He, and G. C. Tepper, "A new coplanar-grid high-pressure xenon gamma-ray spectrometer," *IEEE Trans. Nucl. Sci.*, vol. 52, no. 6, pp. 2932–2939, Dec. 2005.

[13] W. R. Hendee and E. R. Ritenour, *Medical Imaging Physics*., 4th ed. Hoboken, NJ: Wiley, 2002.

[14] F. Sauli, "Micro-pattern gas detectors," *Nucl. Instrum. Methods Phys. Res. A, Accel. Spectrom. Detect. Assoc. Equip.*, vol. 477, no. 1–3, pp. 1–7, Jan. 2002.

[15] F. Sauli, "Gas detectors: Achievements and trends," *Nucl. Instrum. Methods Phys. Res. A, Accel. Spectrom. Detect. Assoc. Equip.*, vol. 461, no. 1–3, pp. 47–54, Apr. 2001.

[16] C. K. Eun and Y. B. Gianchandani, "A microdischarge-based radiation detector utilizing stacked electrode arrays in a TO-5 package," in *Proc. IEEE Int. Conf. Micro Electro Mech. Syst.*, Cancun, Mexico, Jan. 2011, pp. 668–671.

[17] C. K. Eun and Y. B. Gianchandani, "A microfabricated steel and glass radiation detector with inherent wireless signaling," *J. Micromech. Microeng.*, vol. 21, no. 1, p. 015003, Jan. 2011.

[18] M. J. Berger, J. H. Hubbell, S. M. Seltzer, J. Chang, J. S. Coursey, R. Sukumar, D. S. Zucker and K. Olsen, "XCOM: Photon Cross Sections Database," *NIST Standard Reference Database*, Mar. 1998. [Online]. Available: http://physics.nist.gov/PhysRefData/Xcom/Text/XCOM.html

[19] W. M. Haynes, *CRC Handbook on Chemistry and Physics*. Boca Raton, FL: CRC Press, 2008, pp. 12–114.

[20] Bureau of Radiological Health and the Training Institute Environmental Control Administration, Radiological Health Handbook, Rockville, MD: U.S. Dept. Health, Educ., Welfare1970, Jan..

[21] T. Fawcett, "An introduction to ROC analysis," *Pattern Recognit. Lett.*, vol. 27, no. 8, pp. 861–874, Jun. 2006.

[22] C. D. Brown and H. T. David, "Receiver operating characteristics curves and related decision measures: A tutorial," *Chemometrics Intell. Lab. Syst.*, vol. 80, no. 1, pp. 24–38, Jan. 2006.

[23] R. Wolff, "Measurement of the gas constants for various proportional counter gas mixtures," *Nucl. Instrum. Methods*, vol. 115, no. 2, pp. 461–463, Mar. 1974.

[24] A. Sharma and F. Sauli, "First Townsend coefficient measured in argon based mixtures at high fields," *Nucl. Instrum. Methods Phys. Res. A, Accel. Spectrom. Detect. Assoc. Equip.*, vol. 334, no. 2/3, pp. 420–424, Oct. 1993.

Christine K. Eun received the B.S. (*summa cum laude*), M.S., and Ph.D. degrees in electrical engineering from the University of Michigan, Ann Arbor, in 2004, 2006, and 2011, respectively.

She has been funded through various fellowships including the Rackham Merit Fellowship and a fellowship from Sandia National Laboratories, Albuquerque, NM.

Yogesh B. Gianchandani (S'83–M'85–SM'04–F'10) received the B.S., M.S., and Ph.D. degrees in electrical engineering, with a focus on microelectronics and MEMS.

He is currently a Professor with the University of Michigan, Ann Arbor, with a primary appointment in the Department of Electrical Engineering and Computer Science and a courtesy appointment in the Department of Mechanical Engineering. He also serves as the Director of the Engineering Research Center for Wireless Integrated Microsystems. His research interests include all aspects of design, fabrication, and packaging of micromachined sensors and actuators (http://www.eecs.umich.edu/~yogesh/). He has published about 250 papers in journals and conferences and has about 30 U.S. patents issued or pending. He was a Chief Coeditor of *Comprehensive Microsystems: Fundamentals, Technology, and Applications*, published in 2008. He serves several journals as an Editor or a member of the editorial board and served as a General Cochair for the IEEE/ASME International Conference on Micro Electro Mechanical Systems in 2002. From 2007 to 2009, he also served at the National Science Foundation as the Program Director for Micro and Nano Systems within the Electrical, Communication, and Cyber Systems Division.

Dr. Gianchandani is a Fellow of IEEE.